Influence of time-dependent phenomena on translaminar fracture of woven-ply C/PPS laminates above the glass transition temperature

D. Bouscarrat, M. Levesque, Benoît Vieille

Influence of time-dependent phenomena on translaminar fracture of woven-ply C/PPS laminates above the glass transition temperature

D. Bouscarrat[a,b], M. Levesque[b], B. Vieille[a],

[a] *INSA Rouen Normandie, avenue de l'Universite, 76800 St Etienne du Rouvray, France*
[b] *Ecole Polytechnique de Montreal, C.P. 6079, Succ. Centre-ville, Montreal (QC), H3C 3A7, Canada*

Abstract

The time-dependency of damage development and translaminar fracture mechanisms were investigated in 5-harness satin weave carbon fabric reinforced polyphenylene sulfide composites above their glass transition temperature through an approach combining acoustic emission (AE) monitoring and fracture mechanics. Single edge notch specimens from two stacking sequences (quasi-istropic and angle-ply) were subjected to cyclic incremental tensile loading. Tensile tests were carried out for several loading rates or histories featuring creep and/or recovery stages. Both laminates' failure mechanisms do not seem to be influenced by time-dependent phenomena. However, AE monitoring revealed AE activity during creep stages for both stacking sequences, thus highlighting possible time-dependent damage events. If those AE events are indeed related to time-dependent damage, this observation would mean that this damage is only subcritical. Those observations need to be investigated further with acoustic emission coupled to other monitoring tools, such as digital image correlation, in-situ microscopic observations or thermography, to provide a better insight of the physical phenomena associated with the monitored acoustic emission signals.

Keywords: woven-ply composite, thermoplastic, time-dependency, fracture toughness, translaminar fracture, acoustic emission

1. Introduction

Woven-ply composites exhibit damage mechanisms at the micro- (scale of the fibre and matrix), meso- (scale of the bundles) and macroscopic (scale of the laminate) scales. Damage development under tensile loading in woven composite laminates has been investigated by several researchers for thermoset (TS)- [1–6] and thermoplastic (TP)-based composites [7, 8], at Room Temperature (RT). Those studies either focused on on-axis (*i.e.*, the loading is applied parallel to the warp or weft bundles) [1–4, 7, 8] or off-axis (*i.e.*, tensile loading on specimens for which the warp or weft bundles are not aligned with the loading axis) [1, 5, 6, 8] solicitations. Intra-bundle cracking, meta-delamination (*i.e.*, debonding between warp and waft fibre bundles [9]), delamination, fibre-bundle breaking and fibre-bundle pull-out are damage mechanisms typically observed in such composites. The on-axis behaviour is characterized by a fibre-dominated failure. By opposition, the off-axis response is dominated by matrix and fibre/matrix interface behavior, hence generally leading to significant elongation and/or necking [8], as well as significant delamination and fibre-bundle pull-out.

Damage development in woven composites depends on several testing parameters, like temperature and loading rate. An increase in temperature generally leads to an increase in delamination and fibre pull-out for off-axis solicitation [5, 10]. However, no significant differences in failure modes were found for 0° (*i.e.*, aligned with the warp bundles) nor for 90° solicitations [10]. The factors driving temperature-dependent variations are the matrix shear strength and fiber/matrix interface degradation [5, 6, 10]. Futhermore, it has been demonstrated that an increase in frequency reduced the fatigue lives of angle-ply carbon(C)/epoxy woven laminates, but had little effect on C/Polyphenylene Sulfide (PPS) specimens tested under the same conditions (120 °C) [11]. The authors explained this difference by significant autogeneous heating in PPS-based laminates. Such heating increases material ductility and leads to larger plastic strains, locally releasing stress concentrations. The authors have also observed that higher loading frequencies respectively reduced and increased the fatigue lives of quasi-isotropic C/PPS and C/epoxy laminates [12]. The authors justified this result with the combined effects of time-dependent phenomena at lower frequencies that increased the ±45° bundles contribution to the overall behaviour.

A limited number of authors investigated, experimentally, the rate-dependency of interlaminar fracture toughness of TS [13] and TP [14] woven composites. It was concluded that a decrease in interlaminar strain energy release rate (SERR) is associated with an increase in loading rate. However, to the best of our knowledge, no study quantified the effects of time-dependent behaviour in the case of translaminar fracture (*i.e.*, fracture associated with longitudinal tensile failure through fibre failure [15, 16]) in woven composites.

This paper studies the effect of time-dependent phenomena on the translaminar fracture in woven-ply laminates. The material under investigation is a 5-harness satin weave C/PPS. Two stacking sequences were considered: a Quasi-Isotropic (QI) sequence, having a fibre-dominated behaviour, and an Angle-Ply (AP) sequence, characterized by a matrix-dominated behaviour. Tensile tests were carried out on Single-Edge-Notch (SEN)

specimens subjected to different quasi-static loading histories (different loading rates and creep/recovery steps) at 120 °C to investigate the effect of time-dependent phenomena on failure mechanisms and corresponding fracture toughness. An AE set-up was used as an in-situ monitoring of damage development and a potential damage state parameter. The novelty of our work lies in the study of the influence of time-dependent behaviour on translaminar failure of woven laminates through a fracture mechanics framework.

Section 2 describes the framework on which the fracture mechanics analysis is based. The materials and methods used to study the influence of time-dependent phenomena on the fracture behaviours of AP and QI 5-harness satin weave C/PPS composites at 120 °C > T_g are detailed in Section 3. The experimental results are presented in Section 4. Section 5 discusses the results and Section 6 concludes this work.

2. Background information for the determination of fracture toughness parameters

There are different ways to consider fracture mechanics: locally through stress and strain fields around the crack tip, and more globally with an energy criterion like the strain energy release rate [17]. Furthermore, different fracture mechanics frameworks and fracture toughness parameters are used depending on the material behaviour (*e.g.*, linear elasticity or elasto-plasticity).

2.1. Linear Elastic Fracture Mechanics

The Linear Elastic Fracture Mechanics (LEFM) framework relies on the assumption that only small scale yielding (SSY) occurs. In other words, when the plastic zone is very small when compared to the "singularity dominated zone" (SDZ) (*i.e.*, the zone where the crack-tip fields are affected by the presence of the crack). The Stress Intensity Factor (SIF) in mode I (crack opening), K_I, which uniquely characterizes crack-tip conditions, can be computed as:

$$K_I = \sigma^{remote} \sqrt{\pi a_0} f_{cor}(a_0/W), \tag{1}$$

where

$$\sigma^{remote} = \frac{F}{B.W} \tag{2}$$

is the stress far from the crack. F is the applied load, W and B are the specimen's width and thickness, respectively. $f_{cor}(a_0/W)$ is a finite-width correction factor [18]. A function $f_{cor}(a_0/W)$ has been proposed by Gross and Brown [19, 20] for Single-Edge-Notch specimens in Tension (SENT) and is expressed as:

$$f_{cor}(a/W) = 1.122 - 0.231(a/W) + 10.550(a/W)^2 \cdots - 21.710(a/W)^3 + 30.382(a/W)^4. \tag{3}$$

Equation (3) yields an accuracy of 0.5% for $a/W \leq 0.6$ [18]. The SERR, G_I, can be computed from the SIF, K_I, as per:

$$G_I = K_I^2 C_I, \tag{4}$$

where

$$C_I = \sqrt{\frac{1}{2E_xE_y}} \sqrt{\sqrt{\frac{E_x}{E_y}} - \nu_{xy} + \frac{E_x}{2G_{xy}}} \tag{5}$$

for orthotropic materials [15], in which E_x, E_y and G_{xy} are the stiffness in the x and the y directions and the shear modulus in the x-y plane, respectively.

2.2. Elastic Plastic Fracture Mechanics

Elastic Plastic Fracture Mechanics (EPFM) is required when the plastic zone expands to a larger zone since the previous fracture toughness parameters, K_I and G_I, rely on the assumption that plastic strains are small.

The most widely used fracture toughness parameter for elastic-plastic materials is the J-integral [21] and considers an elastic-plastic material as a nonlinearly elastic material. J has a similar mathematical definition that the SERR G_I, but the physical interpretation is different. G_I is defined as the potential energy required for an increment of crack extension within an elastic body, whereas J rather characterizes the difference in elastic-plastic work for specimens with different crack sizes [22]. However, J can still characterize the crack-tip stresses and strains fields. J can be seen as an energy parameter as well as a stress intensity parameter [17].

Several experimental methods have been developped to determine J. Rice et al. [23] proposed the first single-specimen method from the strain energy release rate formulation of J by separating it into elastic, J_{el}, and plastic, J_{pl}, components, as:

$$J = J_{el} + J_{pl}. \tag{6}$$

Sumpter and Turner [24] proposed another expression for J as:

$$J = \eta_{el}\frac{A_{el}}{Bb} + \eta_{pl}\frac{A_{pl}}{Bb}, \tag{7}$$

where A_{el} and A_{pl} are the elastic and plastic works done, respectively. η_{el} and η_{pl} are parameters that depend on the specimen's geometry and loading conditions. B and b are the specimen's thickness and the uncracked ligament length, respectively. A_{el} and A_{pl} are calculated from the load-Load Line Displacement (LLD) curves, as schematized in Figure 1a. Several approaches can be used to determine η_{el} and η_{pl}. Sharobeam and Landes [25] proposed a methodology based on the load separation assumption allowing to represent the load as the multiplication of a material deformation function and a crack geometry function. This method was used [26] to determine η_{pl} for a Single-Edge-Notch (SEN) C/PPS dogbone specimen subjected to a clamped tensile loading. The authors used the compliance method to compute η_{el}. The computed values are summarized in Table 1.

Since the J-integral was developed under the nonlinear elasticity assumption, analyses based on this assumption should not be valid for an elastic-plastic material if unloading occurs. Dowling and Begley [22, 27] were the first to apply

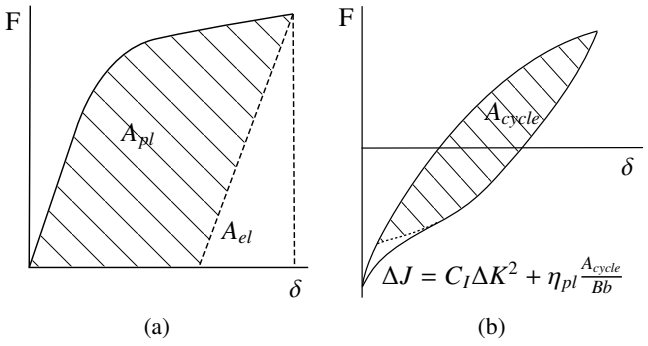

Figure 1: Typical Load-LLD curves for an elasto-plastic material subjected to (a) a monotonic loading and (b) a cyclic loading with a crack closure effect [27]. The y-axis is the applied load, while the x-axis is the displacement between the points where the load is applied. A_{el} and A_{pl} are the elastic and plastic works done, respectively.

Table 1: Values of η_{el} and η_{pl} evaluated in C/PPS angle-ply SEN dogbone specimens subjected to tensile loading at $T > T_g$ [26]

η_{el}	η_{pl}
0.8674	0.7718

the J-integral concept to cyclic loading to predict fatigue crack growth and introduced the ΔJ concept. The ΔJ concept is based on changes in quantities (*e.g.*, displacement, strain, etc.) from a reference state. The onset of crack opening/closure is generally defined as the reference state. Dowling [27] proposed an estimation method similar to Equation 7 using the hysteresis loops of the Load-LLD cycles to compute the plastic component ΔJ_{pl}, as illustrated in Figure 1b, while the elastic component was evaluated using ΔK, which is the equivalent of ΔJ for elastic materials. The applicability of the ΔJ concept as a fracture toughness parameter for cyclic loading is still controversial from a theoretical standpoint. However, the authors noted a good correlation between ΔJ and fatigue crack growth rates.

2.3. Damage and crack propagation monitoring

Several methods can be used to evaluate, qualitatively or quantitatively, the extent of crack development during notch propagation experiments. Crack development can be evaluated through the unloading compliance method [28], Digital Image Correlation (DIC) [29, 30], infrared (IR) thermography [31, 32] or Acoustic Emission (AE) [31, 33–37].

The acquisition of AE signals enables the monitoring of damage events around the crack. One approach consists in tracking damage accumulation and in possibly identifying crack initiation/propagation through any change in AE activity (*i.e*, cumulative events/counts or cumulative energy) [33–36]. Another approach is to directly track the crack propagation through the localization of AE events generated at the crack tip [31, 34, 37]. Some of the previous authors also correlated crack extension with AE activity, either with cumulative hits [33] or with cumulative AE energy [34].

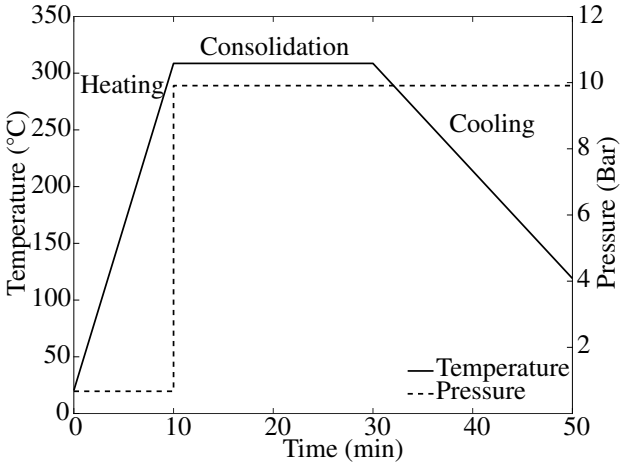

Figure 2: Manufacturing cycle for hot press C/PPS consolidated plates. The consolidation process of seven 0.317 mm thick C/PPS prepregs was achieved at 310 ± 15°C and 10 bars.

AE monitoring has several advantages. The first is that it enables volume measurements of damage propagation, unlike DIC. Therefore, AE analysis may be used to identify the onset of subcritical damage, while DIC detects the onset of macrocrack propagation. Another advantage is that AE enables a possible distinction between the different damage mechanisms occurring within the specimens through data clustering [35].

3. Materials and methods

3.1. Material and specimen geometry

The material under investigation is a carbon fabric reinforced polyphenylene sulfide (C/PPS). The fabric is a balanced 5-harness satin weave (5HS) of carbon fibres (T300 3K) purchased from Soficar. The PPS matrix (Fortron 2014) was supplied by Ticona. Its glass transition temperature is about 95 °C [38].

The quasi-isotropic and angle-ply laminated plates were manufactured by hot press consolidation of 0.317 mm thick prepregs with a volume fraction of carbon fibres equal to 50%. The consolidation process was achieved at 310 ± 15°C and 10 bars, as schematically shown in Figure 2. Two unsymmetric stacking sequences were considered, namely:

- Quasi-isotropic (QI):
  $[(0/90), (\pm 45), (0/90), (\pm 45), (90/0), (\pm 45), (90/0)]$
- Angle-ply (AP): $[(\pm 45)_{3s}(\pm 45)]$

200 mm long specimens were waterjet-cut from 600 × 600 mm^2 plates. The specimen geometry is that proposed in [11, 12], with an additional notch, as illustrated in Figure 3. The single-edge-notch specimens were obtained by machining a central notch with a precision endless diamond wire saw having a radius of 0.085 mm. The notch length was chosen to obtain a ratio $\frac{a_0}{W} \approx 0.3$, a_0 being the initial notch length and W the specimen's width. Ratios ranging from 0.25 to 0.32 were obtained.

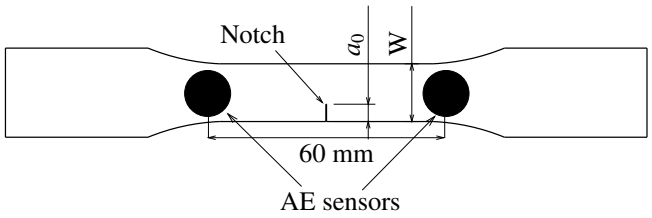

Figure 3: Notched specimen geometry. The dogbone specimens were waterjet-cut from plates. The notches were manufactured with a precision endless diamond wire saw having a radius of 0.085 mm. The notch length to width ratio is about 0.3. The specimen length, width and thickness were around 200, 15 and 2.3 mm, respectively. The two AE sensors were PAC micro80 sensors and were used to spatially filter the AE events.

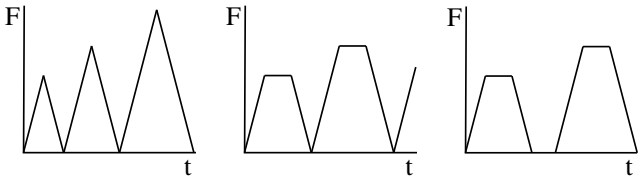

(a) LU (b) LcU (c) LcUr

Figure 4: Illustration of the different incremental tensile loading conditions: (a) Load-unload at 5/50/500 N/s, (b) Load at 50 N/s - 15 minutes creep - unload at 50 N/s and (c) Load at 50 N/s - 15 minutes creep - unload at 50 N/s - 15 minutes recovery

Table 2: Summary of tests carried out on QI and AP laminates for each loading configuration

	Loading	#	B[1] (mm)	W[1] (mm)	Notch ratio[2]	Load increment
QI	LU5	3	2.26	16.27	0.292-0.313	10%
	LU50	3	2.31	16.27	0.289-0.317	10%
	LU500	3	2.25	16.27	0.288-0.305	10%
	LcU50	-	-	-	-	-
	LcUr50	3	2.16	16.27	0.245-0.258	5%
AP	LU5	-	-	-	-	-
	LU50	2	2.33	14.81	0.307-0.317	5%
	LU500	-	-	-	-	-
	LcU50	3	2.36	14.79	0.309-0.318	5%
	LcUr50	3	2.34	14.85	0.304-0.309	5%

[1] Mean values
[2] Min-max values

3.2. Mechanical testing

All the quasi-static tests were performed on a MTS 810 servo-hydraulic testing machine with a 100 kN load cell. The specimens were heated in a MTS 651 environmental chamber at 120 °C. Longitudinal strains were measured by means of a blade-extensometer having a gage length l_0 equal to 25 mm. The SEN specimens were subjected to different incremental force-controlled loading configurations, as shown in Figure 4, namely:

- Load-unload (LU) at 5-50-500 N/s
- Load at 50 N/s - 15 minutes creep - unload at 50 N/s (LcU)
- Load at 50 N/s - 15 minutes creep - unload at 50 N/s - 15 minutes recovery (LcUr)

The LU condition was designed to study the influence of loading rate on damage while the LcU and LcUr conditions were designed to investigate the influence of creep periods on fracture mechanisms. The creep time has to be long enough to exacerbate the viscoelastic effects depending on the testing temperature. In the present case, the temperature is about 120 °C above the matrix T_g. In addition, Albouy has observed that 90 to 95% of the full creep strain occurred within 15 minutes in the case of 24 h creep tests for the same material under the same temperature [39]. As a result, a creep time of 15 minutes is assumed long enough to make a significant difference on the influence of time-dependent effects on damage in the fracture process zone around the crack tip. Creep times of 15 minutes were therefore a good compromise between test duration and the representativeness of the influence of the viscoelastic behavior on crack growth. The solicitation rate for LcU and LcUr configurations was fixed to 50 N/s for both stacking sequences as a compromise between minimizing the machine overshoot and minimizing creep effects during the loading phase. The load levels were determined based on the ultimate load obtained through force-controlled monotonic tensile tests. The ultimate loads are about 5400 N and 3400 N for QI and AP specimens, respectively.

Table 2 summarizes the testing configurations for AP and QI stacking sequences.

3.3. Acoustic emission monitoring

The acoustic emission activity was monitored by means of two PAC micro80 sensors and a PCI-2 data acquisition card. The sensors were separated by 60 mm in a linear arrangement, as shown in Figure 3, to spatially filter the AE events. Every signal was amplified by 20 dB using 2/4/6 pre-amplifiers. The acquisition was done through the software AEwin vE4.70. The acquisition threshold was set to 45 dB and the Peak-Definition-Time/Hit-Definition-Time/Hit-Lockout-Time were set to 30/100/300 μs. Noesis (v7.0) and Matlab software were used for the post-analysis. The following analysis is based on all events localized between the two sensors by keeping the hit from the nearest sensor.

3.4. Determination of fracture toughness parameters

The fracture toughness parameters G_I, for elastic behaviours, and ΔJ, for inelastic ones, were computed.

G_I can be evaluated from Equation (4) using Equations (1) and (5). Its critical value, G_c, can be obtained from the critical stress causing crack extension, σ_c^{remote}. This method was used as a first approximation.

Even though the method to determine ΔJ was developed for elastic-plastic materials under cyclic loading, a similar approach is used in this paper to evaluate the ΔJ-like integral for visco-elasto-plastic materials under incremental load-unload solicitation. Thus, for a visco-elastic-plastic material subjected to a cyclic loading, Equation (7) becomes:

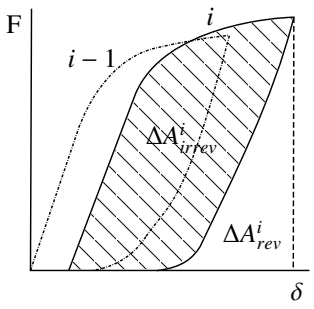

Figure 5: Typical Load-LLD curves for a visco-elasto-plastic material subjected to an incremental load-unload test with no crack closure effect. ΔA_{irrev} is the energy dissipated during a cycle, while ΔA_{rev} is the reversible work.

$$\Delta J = \Delta J_{rev} + \Delta J_{irrev} = \eta_{rev}\frac{\Delta A_{rev}}{Bb} + \eta_{irrev}\frac{\Delta A_{irrev}}{Bb}, \qquad (8)$$

where ΔA_{rev} and ΔA_{irrev} can be evaluated from the Load-LLD curves, as illustrated in Figure 5. It should be noted that no crack closure phenomena, as illustrated in Figure 1b, were observed during the tests. Furthermore, only the irreversible component was investigated because the component J_{el} is only significant at the onset of mechanical loading, whereas the component J_{pl} becomes prominent throughout the test [26]. As a first approximation, η_{irrev} was considered to be equal to η_{pl} (Table 1). This value was determined by Chabchoub et al. [26] for the same material, the same geometry and for identical loading conditions.

4. Results

4.1. Quasi-isotropic laminates

4.1.1. Stress-strain macroscopic response

Figure 6 shows the stress-strain curves for SEN QI specimens subjected to LU (5-50-500 N/s) and LcUr (50 N/s) loadings. This figure shows that QI laminates exhibit a slightly non-linear behaviour, probably due to slight plasticity and progressive damage development as the applied stress approaches the ultimate strength [40]. Furthermore, it appears that QI specimens submitted to the LcUr condition undergo some viscoelastic, viscoplastic and/or time-dependent damage phenomena.

Figure 7 shows the remote stress and strain at failure, σ_r^{remote} and ϵ_r respectively, for the LU (5-50-500 N/s) and LcUr (50 N/s) loading conditions. Figure 7a suggests that σ_r^{remote} for specimens subjected to loading LU500 is slightly higher than those obtained for specimens subjected to loadings LU5 and LU50. In addition, σ_r^{remote} obtained for loading LcUr50 might be higher than those resulting from other loadings due to its slightly lower notch ratio. On the contrary, Figure 7b shows that ϵ_r is insensitive to both loading rate and creep stages.

Table 3 summarizes the number of cycles to failure of all tested specimens for the different loading conditions in the case of QI specimens. It can be seen that the loading configuration does not influence significantly the number of cycles to failure, even for different load increments.

Table 3: Number of cycles to failure for the different loading configurations in the case of QI specimens

Configuration	Load increment	Number of cycles to failure		
		# 1	# 2	# 3
LU5	10%	11	12	11
LU50	10%	10	12	12
LU500	10%	12	11	12
LcUr50	5%	26	25	26

4.1.2. Fracture morphology and strain energy release rate

Figure 8 shows the failure surface of a representative QI specimen. This crack grows self-similarly (*i.e.*, crack propagation occurs in the plane of the initial notch), resulting in an opening mode failure, as illustrated in Figure 8a. The main damage mechanisms involved by this configuration are intra-bundle transverse cracking and breakage of 0° and ±45° bundles. Intra-bundle cracking is not limited to the crack path vicinity, as shown in Figure 8b. Furthermore, it seems that no extensive delamination can be observed while some fibre bundle pull-out can be observed in Figure 8c, especially at the edges of ±45° oriented plies due to edge effects. The main fracture mode is therefore translaminar. It also seems that there is no visible qualitative difference in the fracture morphology between the different loading conditions, suggesting no significant influence of time-dependent phenomena on failure mechanisms.

Figure 9 displays the critical strain energy release rate, G_c for each configuration. The LEFM framework was considered here as a first approximation. These values were computed from Equation (4) and the maximum stress for each test by assuming: *i*) that no prior crack extension occurred and *ii*) that the QI specimens had a macroscopically quasi-isotropic behavior. Figure 9 shows that G_c values exhibit no significant difference between the loading conditions. These results suggest that the influence of time-dependent phenomena on G_c is negligible in QI specimens, whose macroscopic failure mode is fibre-dominated.

4.1.3. AE activity

Figure 10 shows the cumulative events per loading cycle as a function of the maximal remote stress reached during each cycle for the LU5, LU50 and LU500 test configurations. The discontinuous symbols correspond to whole sets of experimental data points, while the continuous lines are exponential regressions. This figure suggests that the higher the solicitation rate, the slower the AE activity as a function of the remote stress is. However, this trend is not that obvious between the LU5 and LU50 configurations due to data dispersion in the LU5 data set. This tendency should be confirmed by additional tests with complementary techniques.

Figure 11 reports the AE activity for the LcUr test configuration for QI laminates. This figure shows that a significant amount of AE events appeared during the high stress level creep stages.

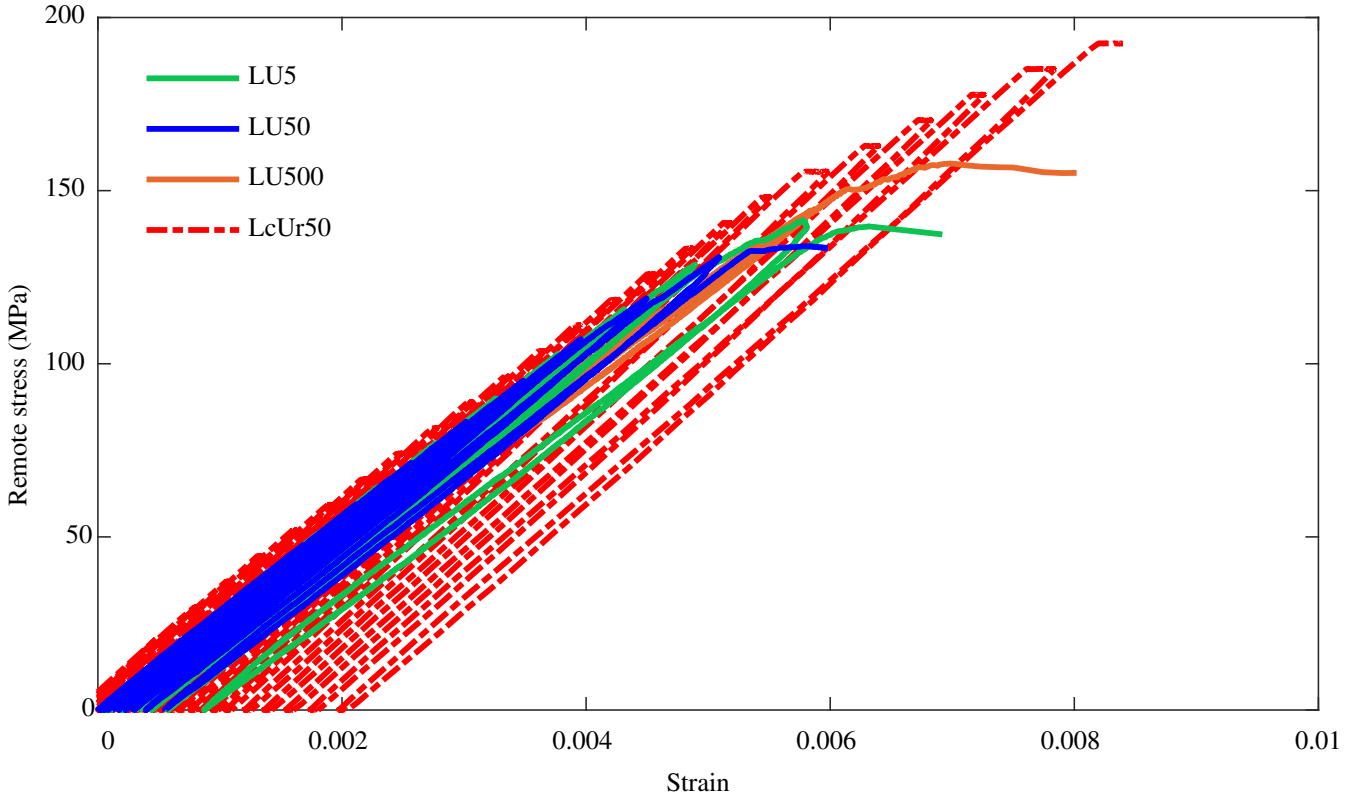

Figure 6: Stress-strain curves for QI SEN specimens subjected to various test conditions at 120 °C: LU5, LU50, LU500 and LcUr50. QI specimens display a slightly non-linear behaviour. However, the inelastic strains remain relatively small. The LcUr50 tests exhibit creep strain and some recovered strain. Those specimens might undergo some viscoelastic, viscoplastic and/or time-dependent damage phenomena.

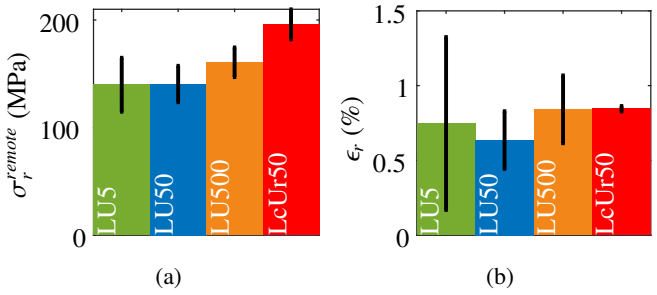

Figure 7: (a) Remote stress and (b) strain at failure of QI SEN specimens subjected to LU5/50/500 and LcUr50 test conditions at 120 °C (the error bars represent the 95% confidence interval). The LU500 test configuration has a slightly higher σ_r^{remote} than those from the LU5 and LU50 test conditions. The higher σ_r^{remote} for the LcUr50 loading might be due to the lower notch ratio more than a time-dependent effect. ϵ_r is not time-dependent.

4.2. *Angle-ply laminates*

4.2.1. *Stress-strain macroscopic response*

Figure 12 reports the stress-strain curves for SEN AP specimens subjected to LU50, LcU50 and LcUr50 loading conditions. AP laminates exhibit a visco-elasto-plastic behaviour promoted by the time-dependent behaviour of the PPS matrix at temperatures higher than its T_g, similarly to what was observed by Albouy [39] in unnotched specimens.

Figure 13 shows the influence of loading conditions on both the remote stress and strain at failure. The figure suggests that σ_r^{remote} and ϵ_r do not seem to be significantly influenced by time-dependent phenomena, as illustrated in Figures 13a and 13b.

Table 4: Number of cycles to failure for the different loading configurations in the case of AP specimens

Configuration	Load increment	Number of cycles to failure		
		# 1	# 2	# 3
LU50	5%	23	22	-
LcU50	5%	20	23	21
LcUr50	5%	21	22	22

Table 4 summarizes the number of cycles to failure of all AP specimens for the different loading conditions. It appears that the loading configuration does not influence significantly the number of cycles to failure.

4.2.2. *Fracture morphology and strain energy release rate*

Figure 14 illustrates the fracture and damage mechanisms occurring within SEN AP specimens. As shown in Figure 14a, it appears that the crack does not grow self-similarly, contrary to what was observed in QI specimens. Indeed, the crack seems to propagate along the (±45°) bundles leading to a mixed-mode I-II (opening-shear) failure, as already observed in the same ma-

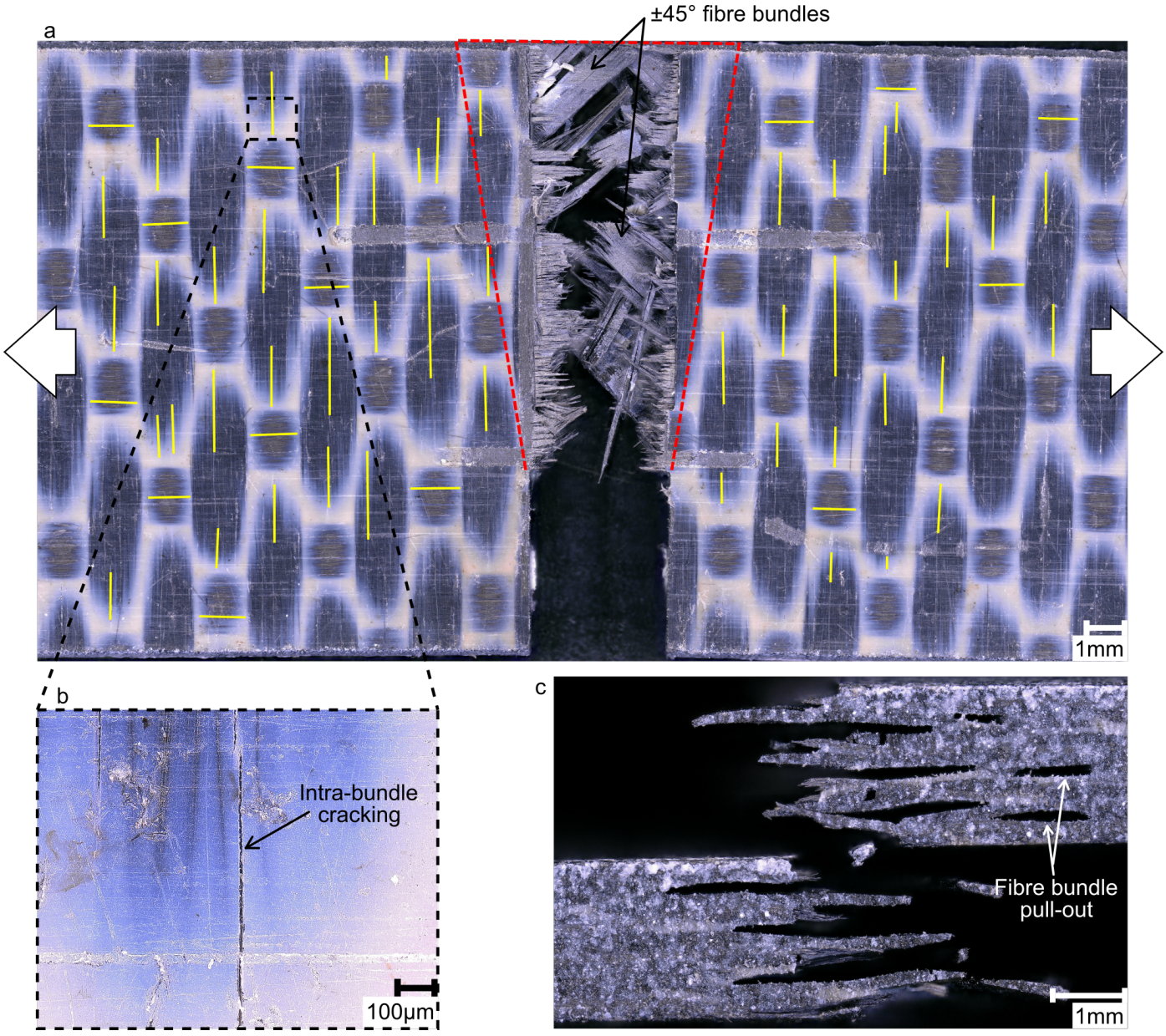

Figure 8: Microscopic observations of (a) the fracture surface, (b) a secondary intra-bundle cracking and (c) the edges of a QI SEN C/PPS specimen subjected to LU500 at 120 °C (the red dot line is an indication of the extent of the fracture process zone and the solid yellow lines indicate secondary intra-bundle cracking). The crack grew in a self-similar manner resulting in a mode I failure. The main damage mechanisms involved are intra-bundle cracking and breakage of bundles. The failure is translaminar at the macroscopic scale. No difference in fracture morphology was observed between the different loading conditions.

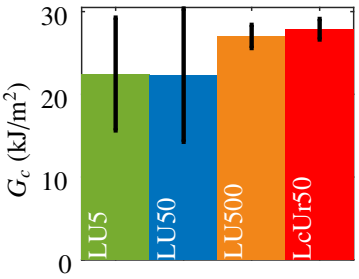

Figure 9: Approximation of the critical strain energy release rate G_c for QI SEN specimens subjected to LU5/50/500 and LcUr50 test conditions at 120 °C (the error bars represent the 95% confidence interval). Those values were computed using Equation (4) and assuming that no prior crack extension occurred before maximum stress, and that the QI specimens exhibited a macroscopically isotropic behaviour with limited inelastic deformation. The figure shows that G_c is not statistically affected by the loading condition. This observation suggests that the influence of time-dependent phenomena on G_c is negligible in QI specimens.

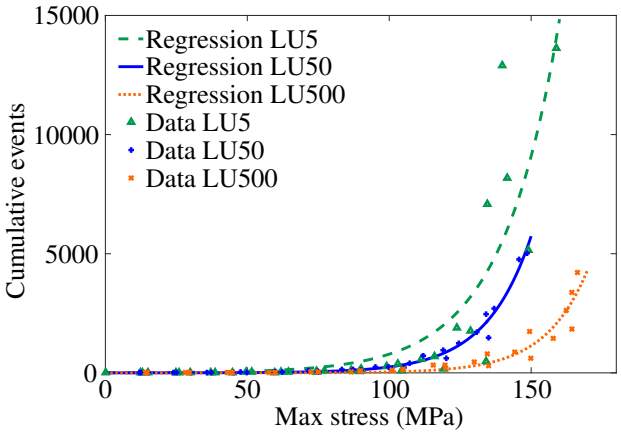

Figure 10: Cumulative events for QI SEN specimens subjected to LU5/50/500 test conditions at 120 °C. The symbols correspond to whole sets of experimental data points, while the continuous lines are exponential regressions. It appears that higher solicitation rates lead to slower AE activity as a function of the remote stress. This tendency is less obvious between the LU5 and LU50 test conditions.

terial [26, 41]. Figures 14a and 14d show that failure occurred after an extensive delamination and meta-delamination leading to fibre bundles pull-outs. Thus, this experimental configuration does not lead to a pure translaminar failure, which is accompanied by damage mechanisms associated with interlaminar failure. Many secondary intra-bundle cracks (Figure 14b), as well as some inter-bundle/interfacial cracks (Figure 14c) away from the main crack's vicinity, are observed, hence revealing a large damaged zone around the crack. Furthermore, no significant difference was observed on the fracture morphology between the different loading conditions, suggesting no substantial influence of time-dependent phenomena on the failure mechanisms at the macroscopic scale.

Figure 15 represents the cumulative ΔJ_{irrev} evolution as a function of the cumulative AE absolute energy, for the different loading conditions. The symbols correspond to the whole experimental data sets, for each test, while the continuous lines

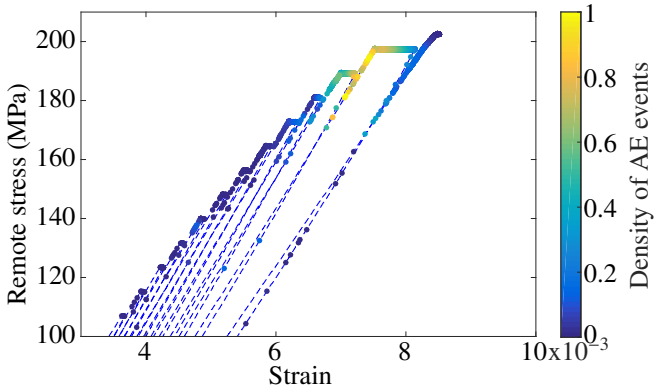

Figure 11: Density of AE events occurring during a LcUr50 test at 120 °C. It appears that a significant amount of AE events occurred during the creep steps for high stresses. These events might result from time-dependent damage.

are exponential regressions. The irreversible component ΔJ_{irrev} was determined at the end of each cycle (excluding the last cycle) using the method defined in Section 3.4 and a corrected uncracked ligament length b' to account for the crack 45° orientation, such as $b' = \frac{b}{cos(\frac{\pi}{4})}$. Complete self-similarity of a fracture process is hardly ever found experimentally in fiber-reinforced polymer laminates. Equation 7 was already used to compute the fracture toughness during non-self-similar propagation [41, 42]. Therefore, Equation 8 is assumed valid to calculate a J-like parameter as a first approximation in order to compare the different loading configurations, regardless the crack propagation path (self-similar or not self-similar). In the present work, the computation of ΔJ is based on the computation of the energy dissipated during a cycle. However, the theoretical validity of this approach should be confirmed. Figure 15 suggests that the data dispersion is quite significant, especially for LcU tests, hence hindering the time-dependent phenomena influence on ΔJ_{irrev}. However, an emerging trend can be guessed from the early stage of the test. ΔJ_{irrev} values computed from the LcUr configuration are higher than those extracted from the LU configurations, while ΔJ_{irrev} values computed from the LcU configurations are positioned between those extracted from LU and LcUr loading cases.

4.2.3. AE activity

Figure 16 shows the cumulative events and cumulative absolute energy per cycle as a function of the maximal remote stress during each cycle. Figure 16a shows that the LU load configuration results in lower amount of AE events than that of the LcU and LcUr loading conditions for stresses higher than 60 MPa. However, the same conclusion is not immediate for stresses close to ultimate failure due to data dispersion. This dispersion could result from a failure mechanism that is not purely translaminar (see Section 4.2.2). These results suggest that there is more damage accumulation in specimens subjected to creep stages. However, conclusions can hardly be drawn about the criticality of damage depending on the loading conditions because there is no significant difference in the evolution of the cumulative absolute energies (see Figure 16b).

Figure 17 shows a similar approach except that the AE ac-

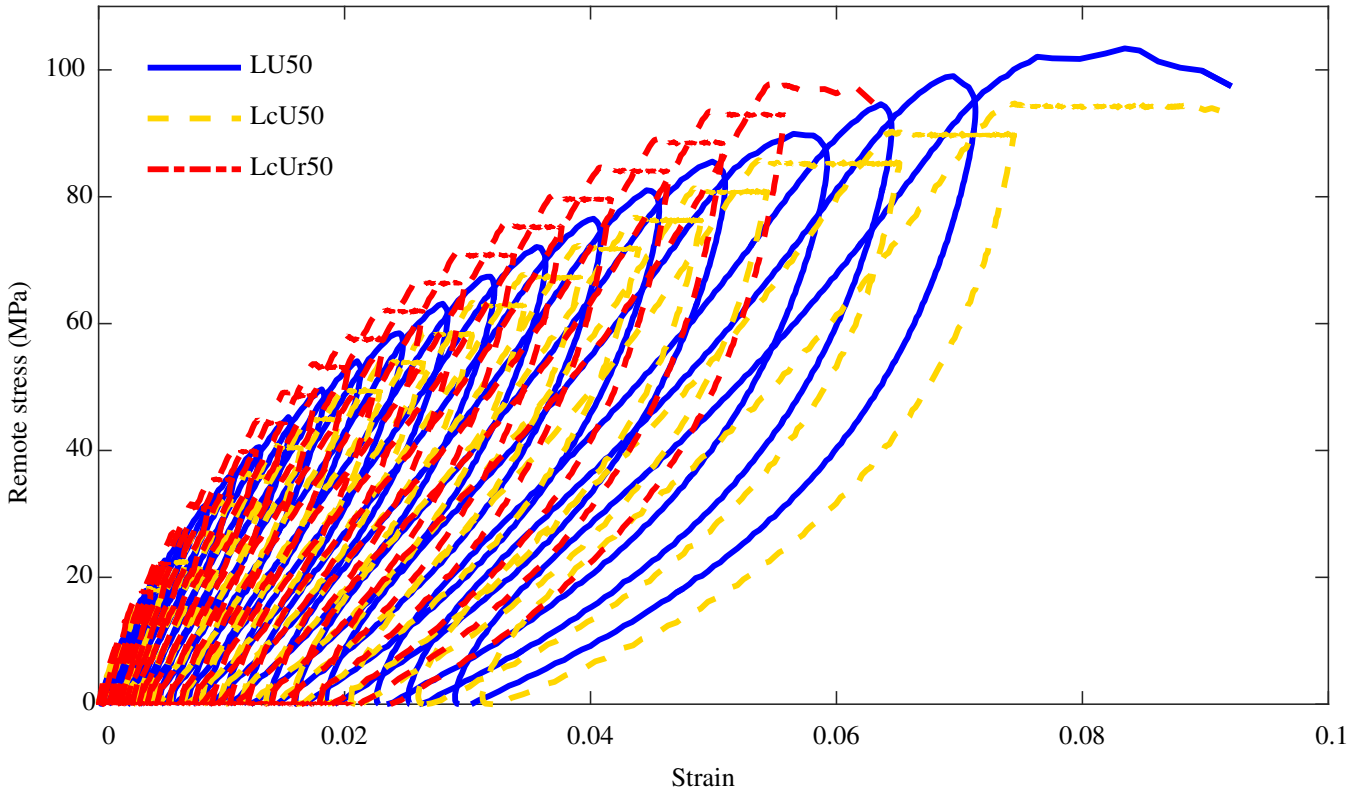

Figure 12: Stress-strain behaviour for AP SEN specimens subjected to various test conditions at 120 °C: LU50, LcU50 and LcUr50. AP specimens display a highly visco-elasto-plastic behaviour.

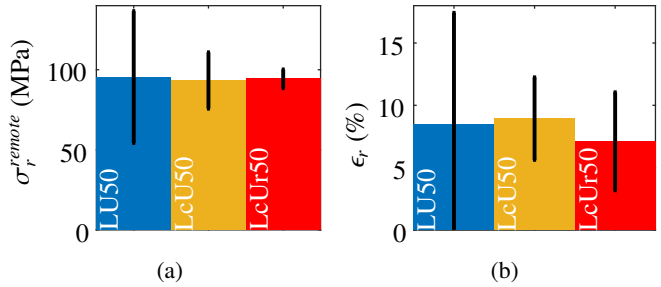

Figure 13: (a) Remote stress and (b) strain at failure of AP SEN specimens subjected to various test conditions at 120 °C (the error bars represent the 95% confidence interval). This figure suggests that the ultimate failure is not influenced by time-dependent phenomena.

tivities were separated during the loading and creep phases. A larger number of events are involved during the creep stages, when compared to the amount of events appearing during the loading phases (Figure 17a). This observation suggests that significant time-dependent damage appears during creep stages. However, the influence of time-dependent damage on the ultimate failure seems insignificant at this stage due to the lack of differences in the cumulative absolute energies, as shown in Figure 17b.

5. Discussion

5.1. QI stacking sequence

The experimental results presented in Figures 6 to 11 suggest that potential time-dependent phenomena have little influence on QI specimens fracture mechanisms, at the macroscopic scale. Though it appears that the LcUr50 configuration has a higher σ_r^{remote} (Figure 7a), this difference can be explained by the shorter crack length. Indeed, the LcUr50 configuration presents a notch ratio significantly different (about -17%) from the other ones. As time-dependent effects are limited in QI specimens, and assuming that QI specimens display linearly elastic and brittle fracture without prior crack propagation, the critical energy release rate G_c should be material-dependent and not dependent on the crack length. Therefore, G_c is a more relevant parameter than the σ_r^{remote} to compare the influence of loading configurations on translaminar failure. This is confirmed in Figure 9 as no significant differences in G_c are observed for the different loading configurations. Furthermore, no significant difference was observed in terms of fracture morphology (Figure 8) and number of cycles to failure (Table 3).

However, AE seems to indicate that the higher the solicitation rate, the slower the evolution of cumulative events as a function of the remote stress is (Figure 10). In addition, the tests conducted with creep and recovery stages show that creep stages may induce some time-dependent damage, as suggested from the AE activity (Figure 11). However, the influence of creep

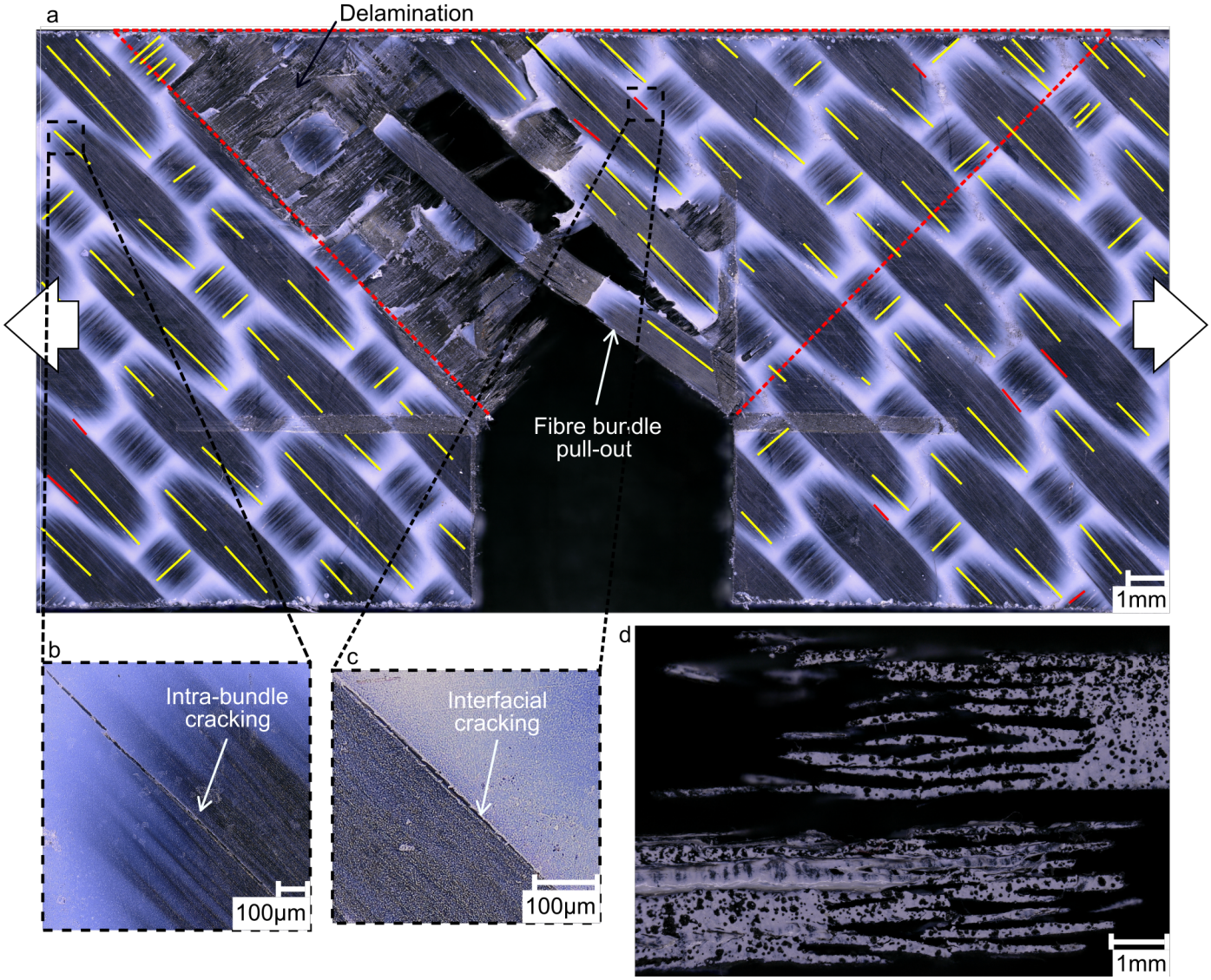

Figure 14: Microscopic observation of (a) the fracture surface, (b) a secondary intra-bundle (continuous yellow line) and (c) secondary inter-bundle/interfacial cracking (continuous red line), as well as (d) the edges of an AP SEN C/PPS specimen subjected to LU50 at 120 °C (the red dot line is an indication of the extent of the fracture process zone). The crack path seems to follow the ±45°) bundles leading to a mixed-mode I-II. An extensive delamination appeared during failure resulting in mixed translaminar-interlaminar failure. No difference in fracture morphology were observed between the different loading conditions.

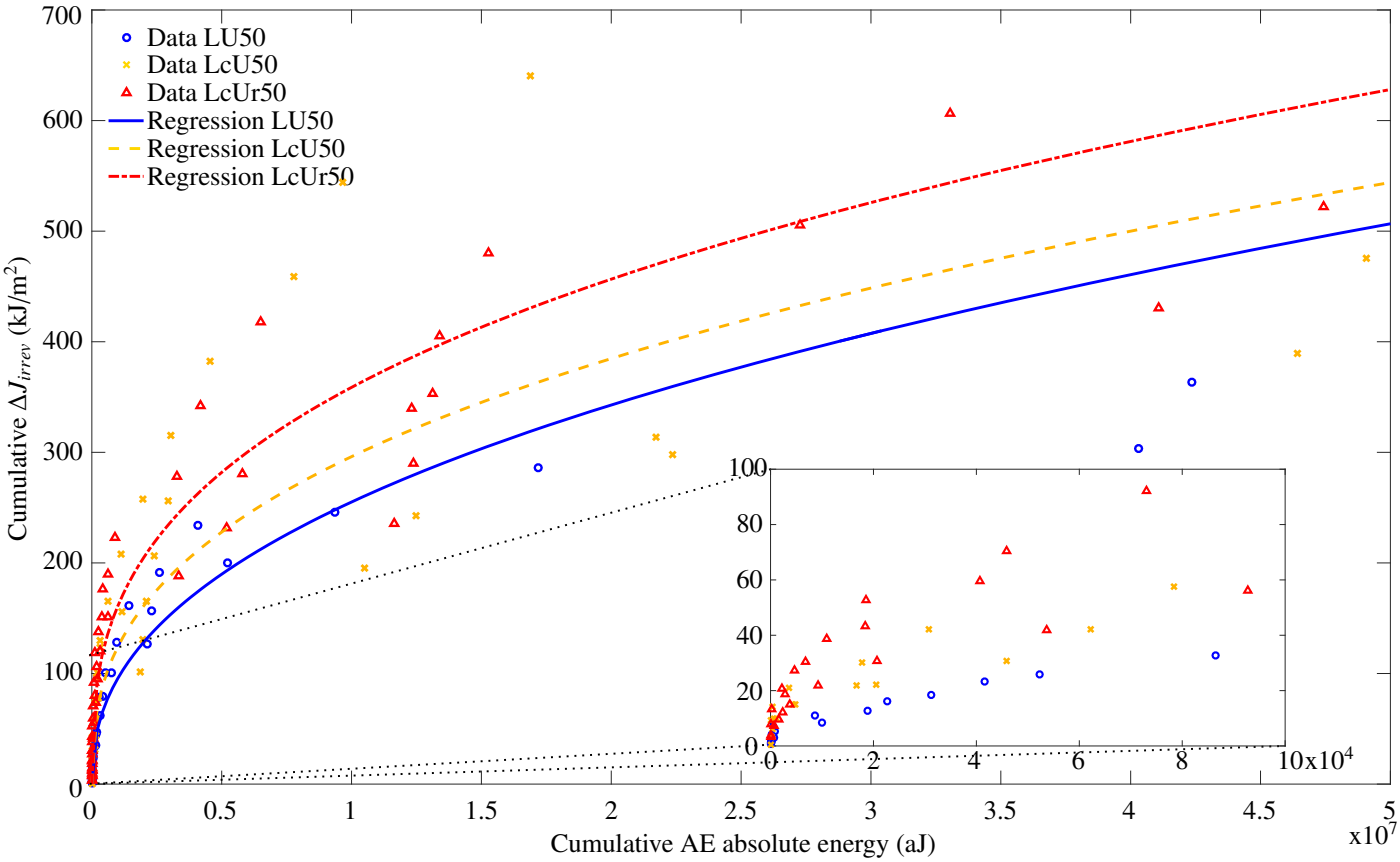

Figure 15: Cumulative ΔJ_{irrev} as a function of the cumulative AE absolute energy for AP SEN specimens subjected to various test conditions at 120 °C. Here, the cumulative AE absolute energy is used as a damage propagation indicator instead of crack extension. The ΔJ_{irrev} are quite scattered, especially in the last cycles. However, an emerging trend can be guessed for the early stage of the tests: $\Delta J^{LU}_{irrev} \leq \Delta J^{LcU}_{irrev} \leq \Delta J^{LcUr}_{irrev}$.

should be further investigated by means of longer creep steps to exacerbate time-dependent damage.

Those observations suggest that translaminar failure mechanisms are not influenced by time-dependent phenomena and possible sub-critical time-dependent damage for QI laminates.

5.2. AP stacking sequence

LU tests at 5 and 500 N/s were not conducted for AP specimens because the number of specimens was limited. However, rate effects are expected to be more significant in AP specimens and should be further investigated. After noticing that (i) the loading rate does not influence the fracture behavior for QI specimens and that (ii) AE events were recorded during creep stages for those specimens, the investigations focused on AP specimens subjected to gradual tensile loading with creep stages at $T > T_g$. The purpose of the present work being to specifically understand the influence of time-dependent effects on translaminar fracture, both viscoelastic and viscoplastic behaviors are exacerbated in such testing conditions.

Both ϵ_r and σ_r^{remote} are not significantly influenced by the loading conditions, which seems to indicate that the critical failure mechanisms are similar, as highlighted by the fractographic analysis (see Section 4.2.2). Those failure mechanisms are mainly bundle/matrix debonding, fibre bundles breakage and meta-delamination. The critical failure mechanisms do not seem to be significantly influenced by time-dependent behaviors involved during creep stages. This could either mean that the creep steps only affect subcritical damage or that the macrocrack propagation is mainly unstable after its initiation, thus leading to similar fracture surfaces. The first observation is supported by the AE activity analysis that suggests an influence of time-dependent phenomena on the onset of damage accumulation and subcritical damage accumulation. Indeed, damage development globally occurs earlier for the LcU and LcUr tests, when compared to what happens during the LU tests, based on the evolution of the cumulative AE events (Figure 16). This observation becomes less obvious close to ultimate failure. This could underline that critical damage accumulation is virtually not influenced by time-dependent phenomena for the studied time scale and that sub-critical damage does not influence the ultimate failure of the specimens, as highlighted by the number of cycles to failure in Table 4. This analysis also points out significant events, and thus probably damage, involved during creep stages, when compared to the events occurring during loading phases (Figure 17).

The analysis of ΔJ_{irrev} as a function of the cumulative AE absolute energy (Figure 15) yields curves whose shape is similar to the conventional J-R curves. However, no definitive conclusion about the influence of the time-dependent phenomena on the fracture toughness can be drawn without a reliable AE crite-

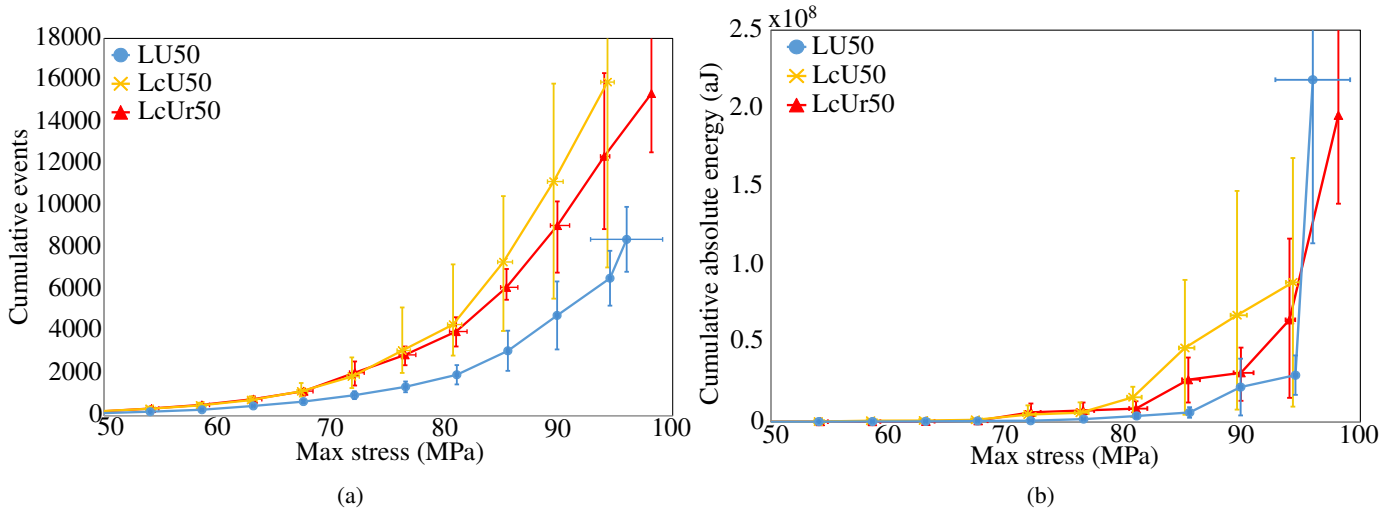

Figure 16: (a) Mean cumulative AE events and (b) Mean cumulative AE absolute energy per cycle for AP SEN specimens subjected to various test conditions at 120 °C (the "error" bars represent the min and max values for each cycle). The LU test condition triggered a lower amount of AE events than the LcU and LcUr load configurations, indicating less damage accumulation. However, the evolution of the cumulative AE absolute energy indicates that the criticality of damage is the same for all the test configurations.

ria for the macro-crack initiation detection. If one considers that a given AE energy reflects a similar damage state between the different configurations, the specimens subjected to the LcUr and LcU loading conditions result in slightly higher values of ΔJ_{irrev} in the early stages of the test due to the visco-elasto-plasticity involved during the creep stages. Such an effect is less obvious after the early stages probably due to the accumulation of more critical damage mechanisms resulting in an extensive and complex fracture process zone mixing translaminar and interlaminar failure mechanisms, as observed in Figure 14. Furthermore, existing or evolutive critical damage, especially interlaminar cracks, could generate some noise signals during the cycles due to friction, which results in potential scatter in the cumulative AE absolute energy. Thus, AE absolute energy might not be the best macro-crack initiation/propagation in this case. Further investigations are necessary to clarify this point.

For now, the influence of time-dependent behaviours involved by 15-minute creep stages does not seem significant on critical damage propagation at the macroscopic scale. The influence of time-dependent phenomena is rather expected to be observed on both micro- or mesoscopic damage initiation and early accumulation due to the presence of matrix-rich areas within the laminates. Indeed, these areas are characterized by locally time-dependent behaviours.

5.3. Comparison between QI and AP laminates

AP specimens exhibited a highly time-dependent behaviour, when compared to QI specimens (see Figures 6 and 12). Furthermore, the AP specimens exhibited a strain at failure 10 times higher than that of the QI specimens. However, the stress at failure is about twice as low as in AP specimens, resulting in greater computed ΔJ_{irrev} in AP laminates, when compared to the values of G_c in QI laminates. This difference is primarily due to different failure mechanisms resulting from specific microstructures. On the one hand, AP specimens display a highly visco-elasto-plastic behaviour that could slow down the propagation of the macro-crack through stress redistribution leading to more extensive secondary damage development around the notch, as illustrated in Figure 14. Furthermore, AP specimens are characterized by extensive delamination, fibre bundle/matrix debonding and pull-out, leading to higher computed ΔJ_{irrev}, when compared to the strain energy release rate of QI specimens, for which interfacial failure is limited. On the other hand, QI specimens, whose macroscopic behaviour is fibre-dominated, are characterized by less plasticity, less secondary damage and a smaller FPZ. This observation is also supported by the AE analysis of the LU50 configuration. Indeed, the failure of AP samples generates slightly more AE events than their QI counterparts, suggesting that more extensive damage develops in AP laminates.

It should be recalled that this fracture mechanics-based analysis is a qualitative comparison. This approach only provides rough estimations of the translaminar fracture toughness of the studied specimens. In addition, QI and AP specimens exhibit different fracture mechanisms, and therefore require specific experimental procedures. QI specimens present elastic-brittle behaviour characterized by unstable brittle failure without prior stable growth, therefore a critical value can be defined unambiguously. However, AP specimens exhibit highly elasto-plastic behaviour characterized by little stable crack propagation and ultimately an unstable propagation. Thus, the fracture toughness results are presented in a form equivalent to a J-R curve for AP specimens, what was not possible for QI specimens due to unstable failure.

6. Conclusion

An original approach combining AE activity monotoring, fractographic analyses and fracture mechanics was considered to specifically address the influence of PPS matrix time-

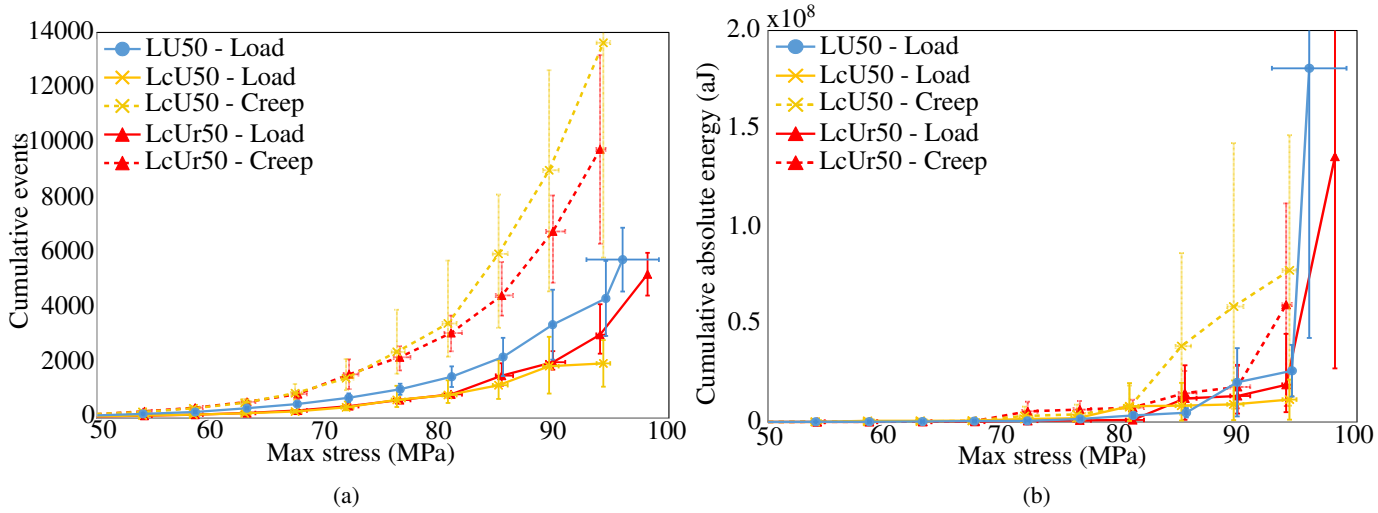

Figure 17: (a) Mean cumulative AE events and (b) Mean cumulative AE absolute energy during loading and creep for AP SEN specimens subjected to various test conditions at 120 °C (the "error" bars represent the min and max values for each cycle). More events appear during the creep stages indicating possible time-dependent damage. However, no significant difference can be observed in the evolution of the cumulative AE absolute energies between the loading and creep phases.

dependent behavior at $T > T_g$ on the translaminar failure of woven-ply PPS-based laminates. To the author's best knowledge, there is no study in the literature that deals with the effects of time-dependent phenomena in the case of translaminar fracture of woven composites. Thus, 5HS C/PPS SEN specimens with two stacking sequences subjected to different loading conditions (different solicitation rates or creep and/or recovery stages) were considered. The purpose was to ponderate the contribution of PPS matrix viscoelastic-viscoplastic behavior to the thermo-mechanical response of C/PPS composites.

From a general standpoint, it seems that damage mechanisms causing ultimate failure are not significantly influenced by time-dependent phenomena for both stacking sequences, though both layups exhibit AE events during the creep stages, which could mean that possible time-dependent damage is only sub-critical. Those AE events needs to be further investigated through a coupled approach with other monitoring tools, such as digital image correlation, in-situ microscopic observations or thermography, to provide a better insight into the underlying physical phenomena. In addition, the investigation of those AE events and the possible crack length changes along with time-dependent effects for longer creep time may be necessary to get a better insight of the influence of visco-elasto-plasiticity on the translaminar failure.

The QI specimens do not exhibit any significant time-dependency from the macroscopic standpoint, probably due to their fibre-dominated behaviour and a very localized time-dependent behaviour. The time-dependent phenomena may influence the early stage of damage or crack development rather than the latter stage (*i.e.*, macro-crack propagation up to the specimens ultimate failure) for AP specimens. The fact that damage growth in AP laminates consists in multiple failure mechanisms that are not purely translaminar may be the reason for which no definitive conclusions can be drawn during the last stage of loading.

Ultimately, further investigations are required, and the experimental protocol should be improved to obtain more quantitative and accurate results. A few improvements can be considered to enhance the quantitative capabilities of the experimental protocol, namely

- Develop of a stable crack propagation. This problem can be solved by using other specimen geometries. Tests under displacement-controlled conditions should be used as force-controlled tests generally lead to an early crack growth instability.

- Use complementary monitoring tools along with AE to follow the macro-crack initiation and its propagation to obtain more reliable quantitative results from the fracture mechanics analyses. This could be achieved using an additional monitoring technique, as DIC or IR thermography. Though AE data presents a significant scatter in this study, such technique provides real-time and in-situ qualitative information regarding damage evolution and the interaction between damage and time-dependent effects at the microscopic scale. In addition, AE activity may be correlated with the macro-crack propagation [33, 34]. To reduce data scattering, additional filters (either feature-based or spatial filters) may be needed to specifically work on events, which originate from the FPZ. Furthermore, an optimization of the experimental procedure resulting in a crack growth with less unwanted interlaminar failure mechanisms may result in less scatter in AE data.

References

[1] M. Karayaka, P. Kurath, Deformation and Failure Behavior of Woven Composite Laminates, Journal of Engineering Materials and Technology 116 (2) (1994) 222–232.

[2] F. Gao, L. Boniface, S. L. Ogin, P. A. Smith, R. P. Greaves, Damage accumulation in woven-fabric CFRP laminates under tensile loading: Part

1. Observations of damage accumulation, Composites Science and Technology 59 (1) (1999) 123–136.
[3] T. Osada, A. Nakai, H. Hamada, Initial fracture behavior of satin woven fabric composites, Composite Structures 61 (4) (2003) 333–339.
[4] S. V. Lomov, D. S. Ivanov, T. C. Truong, I. Verpoest, F. Baudry, K. Vanden Bosche, H. Xie, Experimental methodology of study of damage initiation and development in textile composites in uniaxial tensile test, Composites Science and Technology 68 (12) (2008) 2340–2349.
[5] M. Selezneva, J. Montesano, Z. Fawaz, K. Behdinan, C. Poon, Microscale experimental investigation of failure mechanisms in off-axis woven laminates at elevated temperatures, Composites Part A: Applied Science and Manufacturing 42 (11) (2011) 1756–1763.
[6] J. Montesano, M. Selezneva, Z. Fawaz, C. Poon, K. Behdinan, Elevated temperature off-axis fatigue behavior of an eight-harness satin woven carbon-fiber/bismaleimide laminate, Composites Part A: Applied Science and Manufacturing 43 (9) (2012) 1454–1466.
[7] S. Daggumati, I. De Baere, W. Van Paepegem, J. Degrieck, J. Xu, S. V. Lomov, I. Verpoest, Local damage in a 5-harness satin weave composite under static tension: Part I Experimental analysis, Composites Science and Technology 70 (13) (2010) 1926–1933.
[8] P. Carnevale, TU Delft: Aerospace Engineering: Aerospace Structures and Materials, TU Delft, Delft University of Technology, Fibre-matrix interfaces in thermoplastic composites: A meso-level approach, Ph.D. thesis (Feb. 2014).
[9] T. Fujii, S. Amijima, K. Okubo, Microscopic fatigue processes in a plain-weave glass-fibre composite, Composites Science and Technology 49 (4) (1993) 327–333.
[10] M. Kawai, T. Taniguchi, Off-axis fatigue behavior of plain weave carbon/epoxy fabric laminates at room and high temperatures and its mechanical modeling, Composites Part A: Applied Science and Manufacturing 37 (2) (2006) 243–256.
[11] W. Albouy, B. Vieille, L. Taleb, Influence of matrix ductility on the high-temperature fatigue behavior of off-axis woven-ply thermoplastic and thermoset laminates, International Journal of Fatigue 63 (2014) 85–96.
[12] W. Albouy, B. Vieille, L. Taleb, Influence of matrix ductility on the high-temperature fatigue behaviour of quasi-isotropic woven-ply thermoplastic and thermoset laminates, Composites Part A: Applied Science and Manufacturing 67 (2014) 22–36.
[13] H. Zabala, L. Aretxabaleta, G. Castillo, J. Aurrekoetxea, Loading rate dependency on mode I interlaminar fracture toughness of unidirectional and woven carbon fibre epoxy composites, Composite Structures 121 (2015) 75–82.
[14] S. Mall, G. Law, M. Katouzian, Loading Rate Effect on Interlaminar Fracture Toughness of a Thermoplastic Composite, Journal of Composite Materials 21 (6) (1987) 569–579.
[15] M. J. Laffan, S. T. Pinho, P. Robinson, A. J. McMillan, Translaminar fracture toughness testing of composites: A review, Polymer Testing 31 (3) (2012) 481–489.
[16] G. Bullegas, S. T. Pinho, S. Pimenta, Engineering the translaminar fracture behaviour of thin-ply composites, Composites Science and Technology 131 (2016) 110–122.
[17] T. L. Anderson, Fracture mechanics: fundamentals and applications, CRC press, 2005.
[18] H. Tada, P. Paris, G. Irwin, The analysis of cracks handbook, Vol. 2, New York: ASME Press, 2000.
[19] B. Gross, J. Srawley, Stress-Intensity Factors for a Single-Edge-Notch Tension Speciment by Boundary Collocation of a Stress Function, Tech. Rep. NASA TN D-2395 (1964).
[20] W. Brown, J. Srawley, Plane Strain Crack Toughness Testing of High Strength Metallic Materials, in: Plane Strain Crack Toughness Testing of High Strength Metallic Materials, ASTM International, 1966, pp. 1–129.
[21] J. R. Rice, A Path Independent Integral and the Approximate Analysis of Strain Concentration by Notches and Cracks, Journal of Applied Mechanics 35 (2) (1968) 379–386.
[22] N. E. Dowling, J. A. Begley, Fatigue Crack Growth During Gross Plasticity and the J-Integral, in: J. Rice, P. Paris (Eds.), Mechanics of Crack Growth, ASTM International, 1976, pp. 82–103.
[23] J. Rice, P. Paris, J. Merkle, Some Further Results of J-Integral Analysis and Estimates, in: J. Kaufman, J. Swedlow, H. Corten, J. Srawley, R. Heyer, E. Wessel, G. Irwin (Eds.), Progress in Flaw Growth and Fracture Toughness Testing, ASTM International, 1973, pp. 231–245.
[24] J. D. G. Sumpter, C. E. Turner, Method for Laboratory Determination of Jc, in: J. Swedlow, M. Williams (Eds.), Cracks and Fracture, ASTM International, 1976, pp. 3–18.
[25] M. H. Sharobeam, J. D. Landes, The load separation criterion and methodology in ductile fracture mechanics, International Journal of Fracture 47 (2) (1991) 81–104.
[26] M. Chabchoub, B. Vieille, M. Beyaoui, M. Taktak, M. Haddar, L. Taleb, Determination of J-R curves by load separation criterion in highly ductile TP-based composites under high temperature conditions, Composite Structures 182 (2017) 391–401.
[27] N. E. Dowling, Geometry Effects and the J-Integral Approach to Elastic-Plastic Fatigue Crack Growth, in: J. Swedlow, M. Williams (Eds.), Cracks and Fracture, ASTM International, 1976, pp. 19–32.
[28] ASTM E1820-18a Standard Test Method for Measurement of Fracture Toughness, Tech. rep., ASTM International (2018).
[29] S. Vanlanduit, J. Vanherzeele, R. Longo, P. Guillaume, A digital image correlation method for fatigue test experiments, Optics and Lasers in Engineering 47 (3) (2009) 371–378.
[30] M. Chabchoub, D. Bouscarrat, B. Vieille, C. Gautrelet, M. Beyaoui, M. Taktak, M. Haddar, L. Taleb, Investigations on the mode I translaminar failure and determination of fracture toughness in woven-ply carbon fibers thermoplastic composites at high temperatures, Applied Acoustics 128 (2017) 55–63.
[31] G. Romhany, T. Czigany, J. Karger-Kocsis, Determination of JR curves of thermoplastic starch composites containing crossed quasi-unidirectional flax fiber reinforcement, Composites Science and Technology 66 (16) (2006) 3179–3187.
[32] T. Lisle, M.-L. Pastor, C. Bouvet, P. Margueres, Damage of woven composite under translaminar cracking tests using infrared thermography, Composite Structures 161 (2017) 275–286.
[33] K. G. Dassios, E. Z. Kordatos, D. G. Aggelis, T. E. Matikas, Crack Growth Monitoring in Ceramic Matrix Composites by Combined Infrared Thermography and Acoustic Emission, Journal of the American Ceramic Society 97 (1) (2014) 251–257.
[34] M. Saeedifar, M. Fotouhi, M. Ahmadi Najafabadi, H. Hosseini Toudeshky, G. Minak, Prediction of quasi-static delamination onset and growth in laminated composites by acoustic emission, Composites Part B: Engineering 85 (2016) 113–122.
[35] M. Nikbakht, J. Yousefi, H. Hosseini-Toudeshky, G. Minak, Delamination evaluation of composite laminates with different interface fiber orientations using acoustic emission features and micro visualization, Composites Part B: Engineering 113 (2017) 185–196.
[36] F. Lissek, A. Haeger, V. Knoblauch, S. Hloch, F. Pude, M. Kaufeld, Acoustic emission for interlaminar toughness testing of CFRP: Evaluation of the crack growth due to burst analysis, Composites Part B: Engineering 136 (2018) 55–62.
[37] G. Romhany, T. Czigany, J. Karger-Kocsis, Failure Assessment and Evaluation of Damage Development and Crack Growth in Polymer Composites Via Localization of Acoustic Emission Events: A Review, Polymer Reviews 57 (3) (2017) 397–439.
[38] D. Blond, B. Vieille, M. Gomina, L. Taleb, Correlation between physical properties, microstructure and thermo-mechanical behavior of PPS-based composites processed by stamping, Journal of Reinforced Plastics and Composites 33 (17) (2014) 1656–1668.
[39] W. Albouy, B. Vieille, L. Taleb, Experimental and numerical investigations on the time-dependent behavior of woven-ply PPS thermoplastic laminates at temperatures higher than glass transition temperature, Composites Part A: Applied Science and Manufacturing 49 (2013) 165–178.
[40] B. Vieille, M. Chabchoub, D. Bouscarrat, C. Gautrelet, A fracture mechanics approach using Acoustic Emission Technique to investigate damage evolution in woven-ply thermoplastic structures at temperatures higher than glass transition temperature, Composites Part B: Engineering 116 (2017) 340–351.
[41] B. Vieille, M. Chabchoub, C. Gautrelet, Influence of matrix ductility and toughness on strain energy release rate and failure behavior of woven-ply reinforced thermoplastic structures at high temperature, Composites Part B: Engineering 132 (2018) 125–140.
[42] B. Vieille, Evolution of the strain energy release rate during ductile or brittle failure in woven-ply reinforced thermoplastic laminates under high temperature conditions, Polymer Composites 0 (0).